# Continental Shelf Baroclinic Instability. Part II: Oscillating Wind Forcing

K. H. BRINK AND H. SEO

*Department of Physical Oceanography, Woods Hole Oceanographic Institution, Woods Hole, Massachusetts*

(Manuscript received 2 March 2015, in final form 13 November 2015)

## ABSTRACT

Continental shelf baroclinic instability energized by fluctuating alongshore winds is treated using idealized primitive equation numerical model experiments. A spatially uniform alongshore wind, sinusoidal in time, alternately drives upwelling and downwelling and so creates highly variable, but slowly increasing, available potential energy. For all of the 30 model runs, conducted with a wide range of parameters (varying Coriolis parameter, initial stratification, bottom friction, forcing period, wind strength, and bottom slope), a baroclinic instability and subsequent eddy field develop. Model results and scalings show that the eddy kinetic energy increases with wind amplitude, forcing period, stratification, and bottom slope. The dominant alongshore length scale of the eddy field is essentially an internal Rossby radius of deformation. The resulting depth-averaged alongshore flow field is dominated by the large-scale, periodic wind forcing, while the cross-shelf flow field is dominated by the eddy variability. The result is that correlation length scales for alongshore flow are far greater than those for cross-shelf velocity. This scale discrepancy is qualitatively consistent with midshelf observations by Kundu and Allen, among others.

## 1. Introduction

For a range of continental shelf locations, Kundu and Allen (1976), along with several subsequent investigators (e.g., Winant 1983; Dever 1997; S. Lentz 2015, personal communication), have demonstrated a striking discrepancy between large correlation length scales for middepth subtidal alongshore velocity versus shorter scales for cross-shelf velocity. This order of magnitude discrepancy is far greater than can be accounted for by the natural scale differences for isotropic current variability (e.g., Batchelor 1960).

Brink (2016, hereinafter referred to as B16) proposed that this widely found discrepancy can be explained by the alongshore current being dominated by energetic, ultimately wind-driven flow, but the subsurface cross-shelf velocity (which is very weak for large-scale wind-driven flow) being dominated by small eddies deriving ultimately from baroclinic instability. This instability would occur because alongshore winds drive either upwelling or downwelling circulations that, in turn, tilt isopycnals and so create available potential energy (APE). This

idea is not entirely new; it has been shown that coastal upwelling fronts are expected to be unstable (Barth 1989a,b; Barth 1994; Durski and Allen 2005; and others), but this is a particularly energetic extreme of wind forcing, and the statistical properties of the resulting eddies have not received much attention. On the other hand, there is very little in the literature involving realistic downwelling configurations over the shelf. B16 used a primitive equation numerical model to treat idealized problems where a pulse of alongshore wind invariably leads to the generation of appropriately small-scale (often 1–10 km) eddies over a model continental shelf regardless of the wind direction. Notably, the eddies are comparably energetic in response to either upwelling- or downwelling-favorable winds.

While the B16 approach leads to some insights and reasonable scalings for eddy properties, the model, as configured, is not particularly realistic, especially in terms of the wind forcing; such isolated wind events are not normally found in nature. Many coastal regions, especially those, like the Mid-Atlantic Bight (e.g., Beardsley et al. 1985), not characterized by persistent upwelling, typically undergo a sequence of wind reversals as weather systems pass by. Thus, the present study deals with the somewhat more realistic case of a spatially uniform, temporally sinusoidal wind stress so that the consequences of sustained, reversing wind

*Corresponding author address*: K. H. Brink, Department of Physical Oceanography, Woods Hole Oceanographic Institution, 266 Woods Hole Road, Woods Hole, MA 02543.
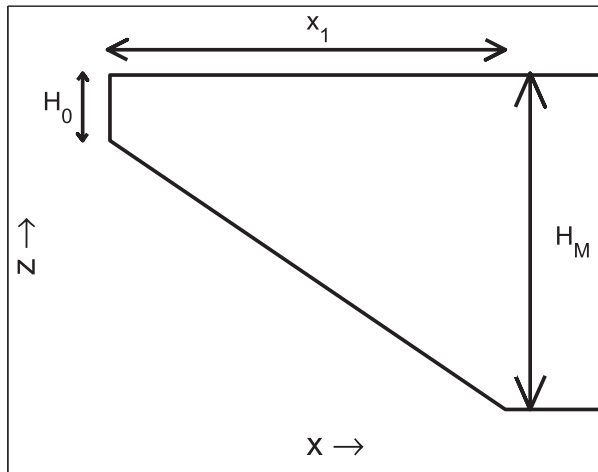E-mail: kbrink@whoi.edu

FIG. 1. Schematic of the model geometry.

forcing can be studied. Using a monochromatic forcing allows assessment of the dependence on forcing frequency, and some ability to relate results in the short-lived forcing of B16. Elimination of potentially complicating effects, such as irregular topography or spatially variable winds, will isolate the role of baroclinic instability. More realistic, broadband wind forcing is the subject of an ongoing study, which will be reported as the third part of the present sequence in the near future. It is worth noting that Durski and Allen (2005) briefly consider time-variable alongshore winds, but they do not include frequent reversals. One might expect potentially different results with reversing winds because alternating upwelling and downwelling would presumably cause the available potential energy required for baroclinic instability to vary radically with time. Further, Flierl and Pedlosky (2007) show that, under some circumstances, baroclinic instability can be enhanced by a fluctuating ambient flow. Here, we seek to explore the consequences of this presumably more realistic wind forcing and learn whether wind-driven baroclinic instability might still be a viable process.

## 2. Methodology

All numerical model runs are carried out using the hydrostatic, primitive equation Regional Ocean Modeling System (ROMS; see, e.g., Haidvogel et al. 2000) in an alongshore cyclic channel configuration. The geometry (Fig. 1) has a coastal wall of depth $H_0 = 5$ m, a sloping region $x_1 = 45$ km wide, and an open offshore boundary at $x = 54.7$ km, where the water has depth $H_M$. The horizontal grid resolution is 0.15 km alongshore and ranges cross shelf from 0.15 km close to shore

up to 0.25 km farther offshore. Density is taken to be a function of temperature only, and the model is initialized with constant stratification. All model runs start from rest and are forced by a spatially uniform alongshore wind stress:

$$\tau_0^y = \tau_A \sin(\omega t), \tag{1}$$

where $|\tau_A|$ is the wind stress amplitude, $\omega$ is the oscillation frequency, and $t$ is the time variable. The winds are initially upwelling (downwelling) favorable for $\tau_A > 0$ ($\tau_A < 0$). There is no surface heat flux. The Mellor–Yamada level 2.5 turbulence closure scheme (e.g., Wijesekera et al. 2003) is used to determine vertical eddy viscosity and diffusivity, and no explicit lateral mixing or diffusivity is applied. The bottom stress $\boldsymbol{\tau}_B$ takes a linear form

$$\boldsymbol{\tau}_B = \rho_0 r \boldsymbol{v}_B, \tag{2}$$

where $r$ is a bottom resistance coefficient, and $\boldsymbol{v}_B$ is the velocity just above the bottom. Further information about the model configuration can be found in B16.

A number of diagnostic quantities are used in the following analysis. These are all based on defining an along-channel mean $\{q\}$, where $q$ is some quantity and $\{\ \}$ represents an average over the entire channel length in the $y$ direction. The deviation from this mean is denoted by $q'(x, y, z, t)$, where $y$ is the along-channel coordinate, and $z$ is the vertical coordinate. Using these definitions, the local (meaning statistics relative to an along-channel mean and as a function of offshore and vertical location) eddy kinetic energy per unit mass is

$$\text{eke}(x, z, t) = \frac{1}{2}\{u'^2 + v'^2\}. \tag{3a}$$

The local energy quantities are then averaged over a cross-sectional area $A$, which ranges from the coast out to $x = W$ (40 km throughout the following) and over all depths, to obtain the spatially averaged eddy kinetic energy

$$\begin{aligned} \text{EKE}(t) &= \frac{1}{2A}\int_0^W \int_{-h}^0 \{u'^2 + v'^2\}\, dz\, dx \\ &= \frac{1}{A}\int_0^W \int_{-h}^0 \text{eke}\, dz\, dx, \end{aligned} \tag{3b}$$

the spatially averaged mean kinetic energy

$$\text{MKE}(t) = \frac{1}{2A}\int_0^W \int_{-h}^0 (\{u\}^2 + \{v\}^2)\, dz\, dx, \tag{3c}$$

and the spatially averaged potential energy

$$\text{PE}(t) = \frac{1}{\rho_0 A} \int_0^W \int_{-h}^{\varsigma} g\rho z \, dz \, dx, \qquad (3d)$$

all per unit mass. In these expressions, $u$ and $v$ are the cross-channel and along-channel velocity components; $\rho(x, y, z, t)$ is the variable portion of density; $\rho_0$ is a constant reference density; $\zeta$ is the free-surface height; $h$ is the undisturbed water depth; and $g$ is the acceleration due to gravity. The spatially averaged available potential energy $\text{APE}(t)$ is calculated as the difference between the actual PE at a given moment and the PE if that same density field were adjusted to have flat isopycnals. This is done using a methodology similar to that of Winters et al. (1995): by sorting the gridded density values and rearranging them into the given bottom configuration so that the densest element lies deepest and so on.

The conversion from potential to kinetic energy is

$$
\begin{aligned}
C_{\text{PE}\to\text{KE}} &= -\frac{g}{\rho_0 A} \int_0^W \int_{-h}^{0} \{w\rho\} \, dz \, dx \\
&= -\frac{g}{\rho_0 A} \int_0^W \int_{-h}^{0} (\{w\}\{\rho\} + \{w'\rho'\}) \, dz \, dx, \quad (4)
\end{aligned}
$$

where the $\{w\}\{\rho\}$ term is associated with conversion from mean potential energy to mean kinetic energy (i.e., up/downwelling or geostrophic adjustment), and the $\{w'\rho'\}$ term is associated with eddy processes. The conversion of mean kinetic energy to eddy kinetic energy is

$$
\begin{aligned}
C_{\text{MKE}\to\text{EKE}} = -\frac{1}{A} \int_0^W \int_{-h}^{0} &(\{v_x\}\{u'v'\} + \{v_z\}\{w'v'\} \\
&+ \{u_x\}\{u'u'\} + \{u_z\}\{w'u'\}) \, dz \, dx, \quad (5)
\end{aligned}
$$

where the terms associated with mean alongshore velocity $\{v\}$ dominate the terms associated with mean cross-shelf velocity $\{u\}$. The term including $\{v_z\}$ is associated with Kelvin–Helmholtz instability, while the $\{v_x\}$ term is associated with barotropic instability.

The dominant along-channel wavelength $\lambda(x, t)$ is calculated from the along-channel covariance of the cross-channel velocity, averaged over a range of depths within 1 km of a nominal $x$ location. The wavelength is defined as 4 times the distance to the first zero crossing of the averaged autocovariance function. This definition is motivated by the earlier stages of instability when the along-channel fluctuations tend to be monochromatic. It is also believed to be a tolerable characterization of the length scale at later stages when the eddy field is far from monochromatic. In addition, the depth dependence in the eddy field is characterized by the ratio of rms vertical shear relative to a rms vertically averaged velocity in the upper half of the water column $\Gamma$ (defined, e.g., by Brink and Cherian 2013). This ratio is $>1$ for strongly baroclinic flow and approaches 0 as flow becomes depth independent.

A sequence of 30 three-dimensional model runs are conducted (Table 1), where stress $\tau_A$, forcing frequency $\omega$, initial buoyancy frequency $N$, bottom slope $\alpha$, Coriolis parameter $f$, and bottom resistance parameter $r$ are all varied in differing combinations. The slope Burger number is $s = \alpha N f^{-1}$. Model runs are conducted long enough to be confident that the maximum area-averaged eddy kinetic energy $\text{EKE}_M$ has been reached: typically 200 to 500 model days long. Although the time to reach a maximum is often long compared to, say, seasonal time scales in the coastal ocean, comparable energy levels are typically obtained within 50 days or less (e.g., Fig. 7). In addition, some model runs are replicated with instabilities suppressed by requiring that conditions do not vary in the alongshore direction.

## 3. Results

### a. Two-dimensional behavior

Before treating the fully three-dimensional problem, it is instructive to review the results in the two-dimensional limit where baroclinic instability is not possible. There is, of course, a considerable literature on two-dimensional wind-driven models (e.g., Kuebel Cervantes et al. 2003). For sinusoidal wind forcing [(1)] and $\tau_A > 0$, an ocean initially at rest and with linear physics alternates between a positive alongshore flow (peaking after one-quarter to one-half period, depending on friction) and quiescent conditions. Run 14 (Table 1; forcing period = 20 days; $f = 0.5 \times 10^{-4}\,\text{s}^{-1}$; $r = 2 \times 10^{-4}\,\text{m}\,\text{s}^{-1}$; $s = 0.48$) is used as the focus of much of the following discussion. This is a relatively low-frequency, weakly damped run with a slope Burger number representative of a steeply sloped midlatitude shelf, such as off northern California. The relatively long, 20-day period allows graphical clarity when plotting 500 days of results. The run is typical in regard to its energetics and (in the three-dimensional case) ultimate instability. During the first half period, upwelling conditions prevail, while during the second half period, downwelling conditions tend to flatten out the isopycnals. Using the more complete physics of the primitive equation model (Fig. 2), this qualitative picture is borne out, but mixing and advective effects (especially in the bottom boundary layer where there are pronounced asymmetries of upslope and downslope flow; e.g., Brink and Lentz 2010) act to leave isotherms sloping upward toward the coast

TABLE 1. Model parameters and summary statistics.

| Run | $f \times 10^4\,\mathrm{s}^{-1}$ | $N^2 \times 10^4\,\mathrm{s}^2$ | $r \times 10^4\,\mathrm{m\,s}^{-1}$ | $\alpha \times 10^3$ | Forcing period days | $\tau_A\,\mathrm{N\,m}^{-2}$ | $\mathrm{EKE}_M \times 10^4\,\mathrm{m}^2\,\mathrm{s}^{-2}$ | $\lambda_M$ km | $L_u^y$ km |
|---|---|---|---|---|---|---|---|---|---|
| 1 | 1.0 | 1.0 | 5 | 2.33 | 20 | 0.02 | 1.2 | 4.1 | 1.5 |
| 2 | 1.0 | 1.0 | 5 | 2.33 | 10 | 0.01 | 0.44 | 9.8 | 2.6 |
| 3 | 1.0 | 1.0 | 5 | 2.33 | 10 | −0.02 | 1.1 | 8.0 | 2.1 |
| 4 | 1.0 | 1.0 | 1 | 2.33 | 10 | 0.02 | 2.2 | 5.1 | 2.1 |
| 5 | 1.0 | 1.0 | 5 | 2.33 | 20 | 0.02 | 6.3 | 6.0 | 1.6 |
| 6 | 1.0 | 1.0 | 5 | 3.88 | 10 | 0.02 | 3.2 | 4.8 | 1.7 |
| 7 | 0.5 | 1.0 | 5 | 2.3 | 10 | 0.02 | 7.1 | 9.8 | 3.0 |
| 8 | 1.0 | 0.5 | 5 | 2.33 | 10 | 0.02 | 0.94 | 4.9 | 1.5 |
| 9 | 0.5 | 1.0 | 5 | 3.88 | 10 | 0.02 | 9.50 | 6.8 | 2.0 |
| 10 | 1.0 | 1.0 | 5 | 2.33 | 10 | 0.04 | 6.1 | 9.8 | 2.8 |
| 11 | 1.0 | 0.25 | 5 | 2.33 | 10 | 0.02 | 0.73 | 2.6 | 1.0 |
| 12 | 1.0 | 0.42 | 5 | 2.33 | 10 | 0.02 | 1.14 | 3.0 | 0.9 |
| 13 | 1.0 | 1.0 | 2 | 1.22 | 10 | 0.02 | 0.99 | 3.8 | 1.3 |
| 14 | 0.5 | 1.0 | 2 | 2.33 | 20 | 0.02 | 23.0 | 14.4 | 5.9 |
| 15 | 1.0 | 1.0 | 10 | 3.88 | 5 | 0.02 | 1.45 | 5.5 | 1.5 |
| 16 | 0.5 | 1.0 | 2 | 2.33 | 20 | −0.02 | 7.2 | 14.7 | 4.4 |
| 17 | 1.0 | 1.0 | 5 | 3.88 | 10 | −0.02 | 2.6 | 3.7 | 1.4 |
| 18 | 0.5 | 1.0 | 2 | 3.88 | 10 | 0.02 | 7.5 | 10.7 | 3.0 |
| 19 | 1.0 | 0.5 | 2 | 3.88 | 20 | 0.02 | 3.7 | 7.6 | 1.8 |
| 20 | 0.5 | 1.0 | 1 | 1.22 | 20 | 0.02 | 8.0 | 14.0 | 5.3 |
| 21 | 0.5 | 1.0 | 5 | 1.22 | 20 | 0.02 | 8.3 | 9.9 | 2.4 |
| 22 | 0.5 | 1.0 | 1 | 3.88 | 10 | 0.04 | 11.0 | 18.4 | 3.4 |
| 23 | 1.0 | 1.17 | 1 | 2.33 | 20 | 0.05 | 73.0 | 12.6 | 3.0 |
| 24 | 1.0 | 1.17 | 10 | 2.33 | 20 | 0.05 | 25.0 | 15.2 | 2.7 |
| 25 | 0.5 | 1.0 | 5 | 2.33 | 10 | 0.04 | 14.0 | 22.1 | 5.6 |
| 26 | 1.0 | 1.0 | 5 | 1.22 | 10 | 0.04 | 3.6 | 4.4 | 1.3 |
| 27 | 1.0 | 1.17 | 1 | 2.33 | 12 | 0.05 | 16.2 | 8.0 | 2.0 |
| 28 | 0.5 | 1.17 | 1 | 2.33 | 12 | 0.05 | 24.0 | 25.3 | 4.4 |
| 29 | 1.0 | 1.17 | 1 | 3.88 | 12 | 0.05 | 33.0 | 6.9 | 2.7 |
| 30 | 0.5 | 1.0 | 1 | 3.88 | 12 | 0.04 | 21.0 | 8.7 | 3.4 |

after one full period (Fig. 2, right panel). This is consistent with vertical mixing combined with greater upslope penetration in the thin upwelling bottom boundary layer (as opposed to slower downslope advection in a thick downwelling boundary layer). After a much longer time, for example, after 9.5 and 10 wind cycles, the structures differ very little from those after 0.5 and 1 cycles (Fig. 2) other than that the surface mixed layer is 5–10 m deeper. In terms of available potential energy (which can be thought of as a gross measure of the degree to which isotherms tilt), the APE reaches a peak after about half a forcing period (Fig. 2, left panel, and Fig. 4, upper panel) but does not decrease to zero after a period. In fact, the envelope of APE continues to adjust toward higher values over time, although the rate of increase decreases noticeably (Fig. 4). The phase of the APE oscillations is stable in the sense that the local maxima all occur at the end of the upwelling (positive) phase of the wind forcing, that is, near days 10, 30, 50, and so on (the times that are denoted by colored symbols in Fig. 4).

When $\tau_A < 0$, there is initially downwelling, followed by upwelling. The result is that near-bottom isotherms are depressed during the first half of the cycle and then upslope flow tends to make the isotherms flatter. Again, there are bottom boundary layer asymmetries, and the initial state is not restored (Fig. 3); water is upwelled near the bottom by the end of a full forcing cycle. Once again, APE generally increases with each forcing cycle after roughly the first 100 days (Fig. 4). In this case, the APE phase adjusts from the initial cycle, where APE peaks after half a period (at the end of downwelling) to a later equilibrium (after about day 100) when the maximum APE occurs at the end of the upwelling phase (note the colored symbols; Fig. 4, lower panel).

Thus, after an initial adjustment stage, the APE cycle evolves in all cases so that the sequential APE maxima all occur near the end of the upwelling phase (Fig. 4). This energetic adjustment is accompanied by changes in the alongshore flow, in the two-dimensional case at least (Fig. 5). For example, with $\tau_A > 0$ the depth-averaged alongshore flow $\langle v \rangle$ at $x = 25$ km initially alternates between positive and near-zero flow, but the initial evolution is rapidly "forgotten" in the sense that $\langle v \rangle$ quickly begins to alternate between positive and negative values,
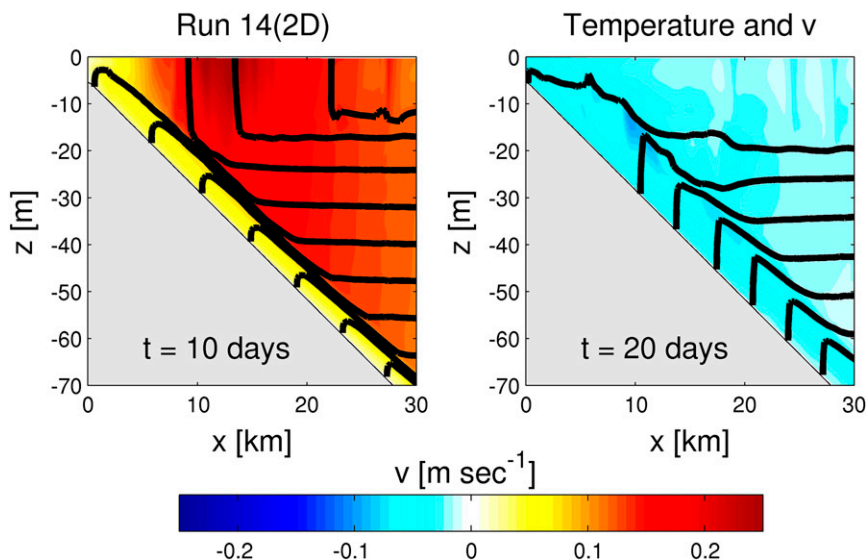
FIG. 2. Temperature (heavy contours, contour interval = 0.5°C) and alongshore velocity (color) at the end of (left) the initial, upwelling, half of the first forcing cycle and (right) a complete forcing cycle. The runs are carried out for the two-dimensional version of run 14 ($\tau_A > 0$), which has a 20-day forcing period.

although an asymmetry remains. The runs with $\tau_A < 0$ adjust more slowly but appear to approach the same pattern as when $\tau_A > 0$. In any case, given hundreds of days, the two-dimensional flow and patterns appear to "forget" their initial conditions and reach a similar state that is characterized by a rectified time-mean flow and wind-driven fluctuations.

The cycle-mean, depth-averaged alongshore velocity at $x = 20$ km late in either run is about 0.05–0.1 m s$^{-1}$ (Fig. 6). One potential explanation for a mean flow is

topographic rectification (e.g., Loder 1980; Brink 2011), where an oscillating cross-shelf flow drives a time-mean alongshore flow. However, repeating these runs with an identical configuration but with much weaker stratification ($N^2$ smaller by a factor of 12) yields a mean alongshore flow that is two orders of magnitude weaker. The weaker stratification also coincides with adjustment times that are about a factor of 5 shorter. A topographically rectified flow's magnitude should not depend so strongly on stratification (Brink 2011), so this
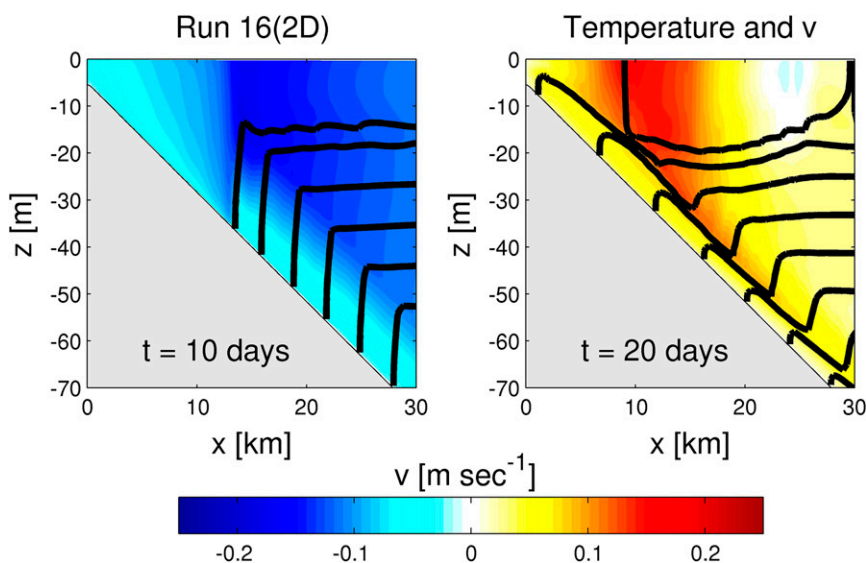


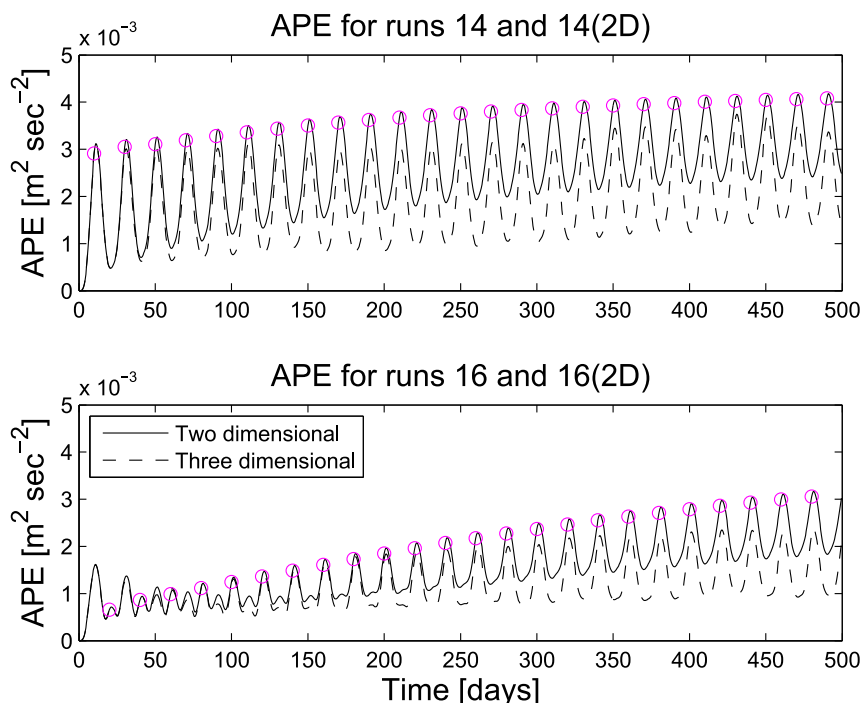FIG. 3. As in Fig. 2, but for run 16 ($\tau_A < 0$).

FIG. 4. Area-averaged (over the inner 40 km of the model domain) available potential energy per unit mass for the two-dimensional (solid line) and three-dimensional (dashed) versions of run 14 (upper panel), which has $\tau_A > 0$. That is, the run begins with upwelling and then downwelling. The lower panel is the same information for run 16, which has $\tau_A < 0$, that is, the run begins with downwelling. Colored symbols are placed for reference at the end of the upwelling phase of each forcing cycle.

mechanism is probably not relevant here. It appears that the reason for the unimportance of this mechanism is that the depth-averaged cross-shelf flow is nearly zero at all times (as must be the case in a two-dimensional, wind-driven model where surface Ekman transport is very nearly balanced by deeper onshore fluxes at all locations). This in turn means that near-surface and near-bottom cross-shelf eddy fluxes of alongshore momentum cancel.

It appears instead that the mean alongshore flow is associated with the asymmetries of mixing and advection during the upwelling and downwelling wind phases. These drive a long-term adjustment toward an upwellinglike (sloping upward toward the coast) temperature field (Fig. 6) regardless of the sign of $\tau_A$. A thermal wind balance is then consistent with the positive alongshore mean flow. Consequently, the very long model adjustment times (e.g., Fig. 5) are evidently associated with a slow decrease of near-bottom temperatures associated with mixing and the asymmetry in bottom boundary layer flow.

The long-term behavior of the two-dimensional system is discussed in detail here because very similar evolution, in terms of phasing and mean flow, is found in

the three-dimensional case where baroclinic instability is present. The two-dimensional results thus highlight aspects of the full solution that are independent of the presence of three-dimensional instabilities.
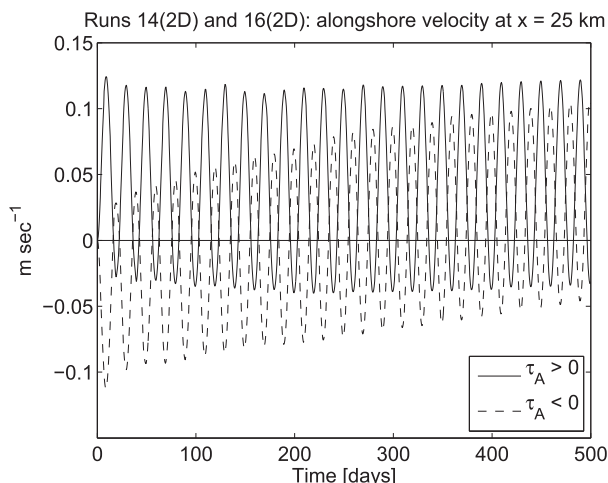


FIG. 5. Depth-averaged alongshore velocity at $x = 25$ km for two-dimensional runs 14(2D) (solid line: $\tau_A > 0$) and 16(2D) (dashed line: $\tau_A < 0$).
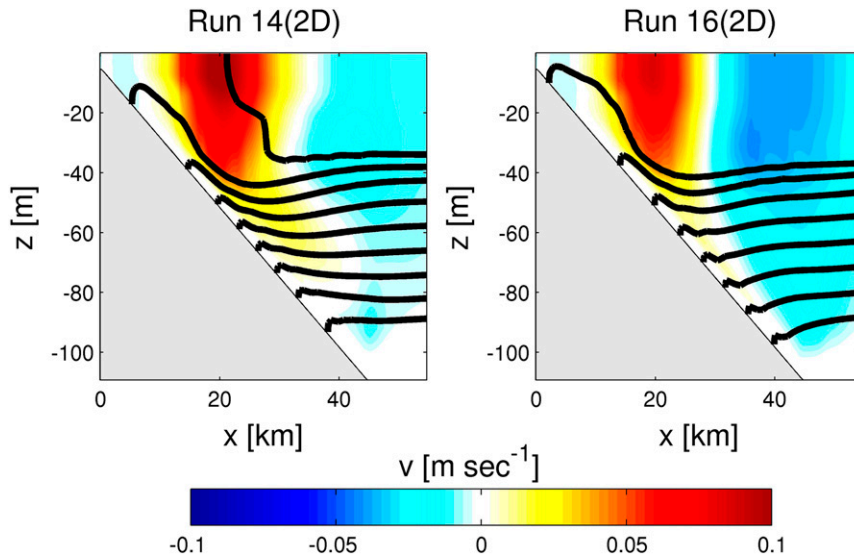
FIG. 6. Mean temperature (contour interval = 0.5°C; heavy contours) and alongshore velocity (color) averaged over the last forcing period (days 481–500) for the two-dimensional versions of runs 14(2D) ($\tau_A > 0$) and 16(2D) ($\tau_A < 0$).

## b. Three-dimensional case

Every three-dimensional model run demonstrates the growth of dominantly baroclinic instabilities; no stable cases were found. Of course, the eddy amplitudes, length scales, and growth rates do vary considerably from one run to another. One representative run (14; Table 1) is here treated in some detail before parameter sensitivity is discussed.

The initial development of the system (before alongshore variations become apparent around day 8; see Fig. 7) is essentially identical to the two-dimensional case, but differences in the APE pool quickly become apparent (Fig. 4, upper panel). In the two-dimensional case, peak APE continues to increase with time, albeit increasingly slowly, while in the three-dimensional case, the peak APE ceases to grow regularly with time, and APE is always less than for the two-dimensional case. This result is not at all surprising; in the three-dimensional case, baroclinic instability releases APE and so restrains its continued growth.

Spatially averaged EKE (Fig. 7) cycles through high and low values with each period. The sequential peak values are found, for example, at days 451, 471, and 490, that is, just after the end of the upwelling phase of each cycle. The minima never reach zero; the eddy field is modulated with the forcing, but it is not extinguished at any time. Interestingly, typical EKE magnitudes are always about an order of magnitude less than those of either MKE or APE. Although the EKE variations show some tendency to repeat from cycle to cycle, their

evolution is far from regular. This is, of course, not surprising given that EKE is a diagnostic of a time-evolving finite-amplitude eddy field.

The time of maximum EKE $t_M$ (411.5 days) is chosen for computing further diagnostics. By this time, the eddy field is well developed, although the larger-scale, directly wind-forced alongshore-averaged alongshore flow $\{v\}$ tends to dominate the overall flow patterns (Fig. 8) except when $\{v\}$ cycles near zero. The eke (Fig. 9) is concentrated in the upper 30 m of the water column and reaches a maximum at the surface at $x_M = 18.6$ km. For comparison, the mixed layer depth at this offshore location is about 27 m. The eke concentration near the surface over roughly a mixed layer depth is typical of all runs. The alongshore wavelength $\lambda(x_M, t)$ (Fig. 7) varies considerably over time, but $\lambda(x_M, t_M) = \lambda_M = 14.4$ km and $\Gamma = 0.81$ for run 14. In many cases such as this one, $\lambda(x_M, t)$ half a period after the peak is larger (16.5 km in this case) and $\Gamma$ is somewhat smaller (0.46), while EKE is lower ($1.64 \times 10^{-4}$ m$^2$ s$^{-2}$). Further, the location of peak eke has shifted offshore to $x = 39.8$ km at $t = 421.5$ days. The point is that although the eddy field is continuously active, the eddy field's properties vary substantially with time and offshore location.

The conversion rates among the different energy pools shed light on the processes involved. Potential energy variations (not shown) are simply associated with the upwelling/downwelling circulation, while the effects of mixing and baroclinic instability (transfer to EKE) are very small in comparison. MKE variations are primarily associated with wind input and
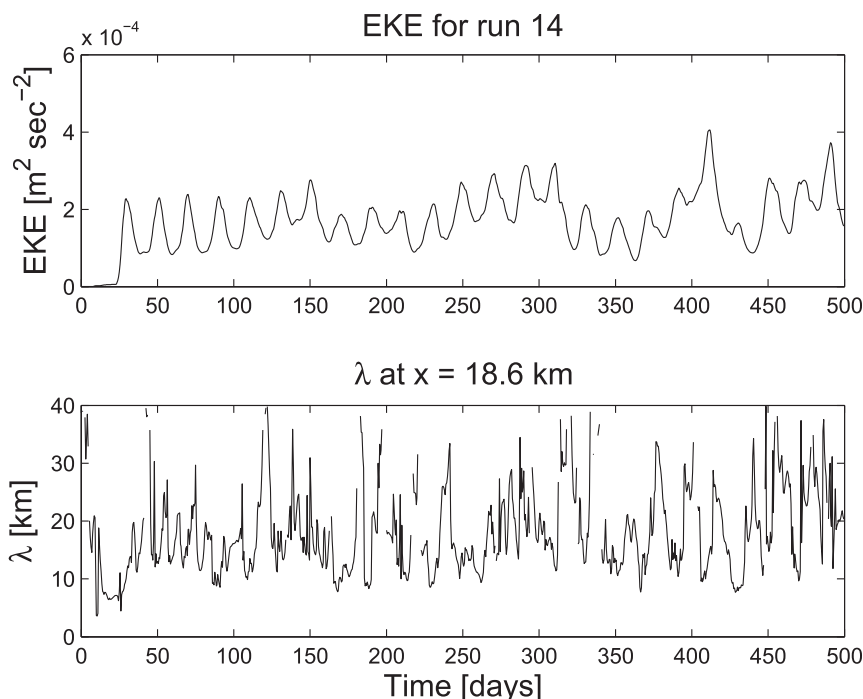
FIG. 7. (top) Time series of spatially averaged eddy kinetic energy per unit mass and (bottom) along-channel wavelength at $x = 18.6$ km for run 14. In the lower panel, gaps occur in the unrealistic case where the estimated wavelength is greater than the channel length.

frictional dissipation. The exchange of MKE with PE is substantial but oscillatory, so there is little net exchange over one cycle. The exchange of energy with EKE is small compared to these other terms. EKE variability (Fig. 10) is dominated by the eddy transfer $\{w'\rho'\}$ from potential to kinetic energy, the term associated with baroclinic instability. This term is positive during all phases of the forcing, although it is generally largest at the end of the upwelling phase of the wind driving. Consistently, across all runs, the mean to eddy kinetic conversion associated with vertical shear $[\{v_z\}\{w'v'\}$ in (5)] is positive most of the time and clearly contributes, in a secondary way, to the otherwise baroclinic instability. The mean to eddy kinetic energy conversion associated with horizontal shear $[\{v_x\}\{u'v'\}$ in (5), the term associated with barotropic instability] fluctuates irregularly and changes sign frequently. It appears to make little net contribution to the energetics. Finally, eddy dissipation, associated both with bottom stress and losses in the bottom boundary layer, consistently removes EKE, albeit at an irregular rate. Thus, the eddy energetics for this and all other runs are dominated by baroclinic instability, dissipation, and sometimes Kelvin–Helmholtz-type instability.

Now consider the time series of depth-averaged velocity components at $x = 30$ km (75 m isobath) and, arbitrarily, $y = 0.15$ km (Fig. 11). The depth-averaged

alongshore flow $\langle v \rangle$ varies roughly sinusoidally with time, although a good deal of raggedness associated with the eddy field is evident. In contrast, the depth-averaged cross-shelf velocity $\langle u \rangle$ varies on much shorter time scales than those of the forcing, and the variations appear chaotic to the eye. The same contrast between $\langle u \rangle$ and $\langle v \rangle$ is found throughout the sloping bottom region; the alongshore flow is dominated by the large-scale
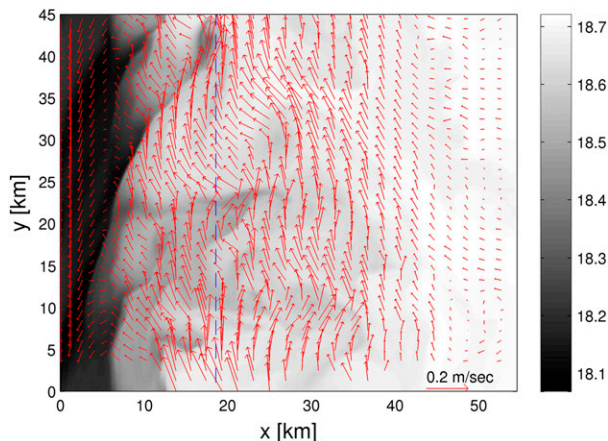


FIG. 8. Surface velocity (arrows) and temperature (shading) for run 14 at $t = 411.5$ days (the moment of maximum eddy kinetic energy). The dashed blue line is located at $x_M = 18.6$ km.
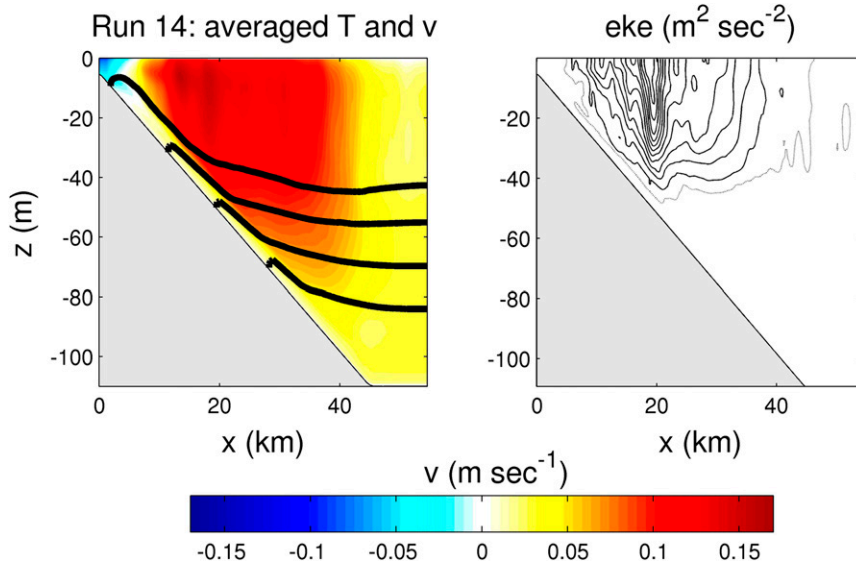
FIG. 9. Results from run 14 at time $t_M$ = 411.5 days. (left) Along-channel averages of temperature (contour interval = 1°C) in heavy contours and alongshore velocity (color). (right) Local eddy kinetic energy eke. The contour interval is $2 \times 10^{-4}\,\mathrm{m^2\,s^{-2}}$ for the solid black contours, and the lighter contour is $1.0 \times 10^{-4}\,\mathrm{m^2\,s^{-2}}$. For comparison, the mixed layer thickness at $x = 19$ km is 27 m.

direct wind forcing, but the depth-averaged cross-shelf flow is not. Depth averaging in the presence of along-shore uniform forcing, however, removes the directly wind-forced component of $u$. For example, near the surface, there is a large-scale, relatively sinusoidal Ekman component of the cross-shelf velocity that, for some runs, is comparable to the eddy variability. Thus, at some (but not all) depths, there can be a substantial large-scale contribution to $u$. Because the wind forcing is spatially uniform, $\{\langle u \rangle\}$ has to be nearly zero (i.e., flow is two-dimensional when averaged alongshore), so that focusing on $\langle u \rangle$ filters out the Ekman components and so resolves only the chaotic component of cross-isobath flow. Finally, the standard deviations of $\langle u \rangle$ and $\langle v \rangle$ for this plot are 0.013 and 0.049 m s$^{-1}$, respectively. Thus, consistent with the argument in the introduction of B16, a typical magnitude for fluctuating cross-shelf currents is smaller than that for alongshore currents but not nearly as small as expected based on a long-wave argument, which would suggest that $\langle u \rangle$ approaches zero in this case (because the wind and topography have in-finite alongshore scale).

The alongshore autocorrelation functions for velocity components and free-surface height versus alongshore separation are calculated at $x = 30$ km ($h = 75$ m) using the last 270 days of the model run. These are computed for a range of alongshore lags starting at 0.5 km and extending out to half the channel length. Because of the cyclic channel, larger lags actually become shorter

because of the reentrant geometry. Thus, instead of using larger $y$ lags, a new set of lagged correlations are calculated starting at half the channel length with a 0.5-km separation. The resulting correlation values (discrete symbols in Fig. 12, left panel) are then averaged
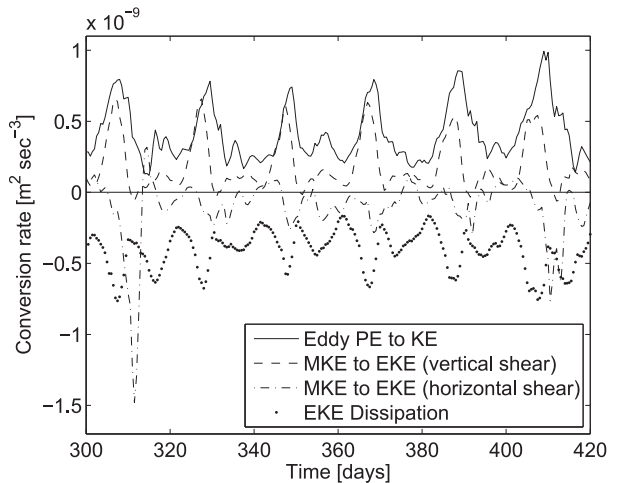


FIG. 10. Time series of area-averaged eddy energy conversions per unit mass for run 14. For clarity, only 120 days of the run are shown. Eddy PE to KE is the $\{w'\rho'\}$ term in (4), and the shear conversion terms are from (5). The dissipation term includes both bottom stress and interior dissipation, which are comparable in magnitude. This plot includes only the most important energy conversion terms, for example, terms associated with fluxes through $x = W$ are not shown.
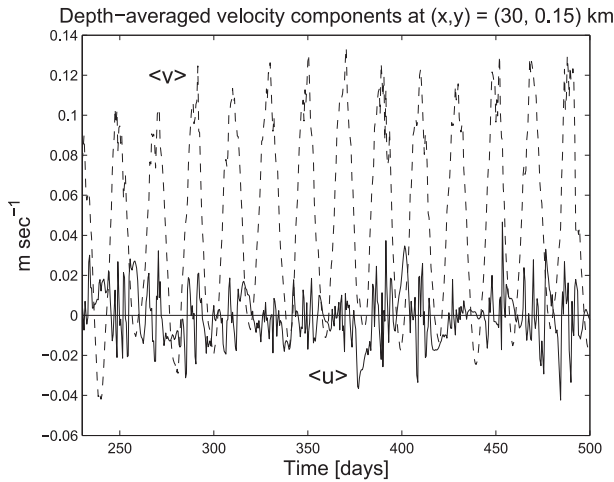
FIG. 11. Depth-averaged alongshore velocity $\langle v \rangle$ (dashed line) and cross-shelf velocity $\langle u \rangle$ (solid line) at $(x, y) = (30, 0.15)$ km for run 14. The maximum EKE occurs at $t_M = 411.5$ days. The standard deviations of $\langle u \rangle$ and $\langle v \rangle$ are 0.013 and 0.049 m s$^{-1}$, respectively.

in 2-km bins to create a smoothed curve. The resulting correlation functions clearly show that free-surface height $\zeta$ and alongshore velocity $\langle v \rangle$ are well correlated over alongshore scales much greater than 20 km. In contrast, the cross-shelf velocity component $\langle u \rangle$ becomes uncorrelated at an alongshore separation of about 7 km and is then weakly negatively correlated for larger scales. This negative side lobe is a familiar result for the velocity component perpendicular to the separation vector in two-dimensional, nondivergent flows (e.g., Batchelor 1960). For comparison, the tabulated

alongshore wavelength $\lambda(x_M, t_M)$ is 14.4 km. The alongshore scale for $\langle u \rangle$ tends to increase with distance offshore (Fig. 13), but the trend is gradual and not monotonic. Cross-shelf variations in the length scale for $\langle v \rangle$ are not generally noticeable. Thus, the scale contrast for alongshore and cross-shelf flow is found across the entire domain of interest. On the other hand, the relative strength of $\langle u \rangle$ and $\langle v \rangle$ (Fig. 13, upper panel) does vary substantially across the shelf, with $\langle u \rangle$ unsurprisingly suppressed near the coast.

The model results beg to be compared to the comparable figure in Kundu and Allen (1976) (Fig. 12, right panel), showing correlations as a function of alongshore separation over the Oregon shelf for middepth flow. The figures are quite comparable in that the $u$ correlation scales are similar and that $v$ is correlated over scales exceeding 20 km. Some caution is required in the comparison. For example, the mooring observations only spanned about 2 months, so there is some statistical uncertainty in the correlations, and the exact values of $u$ correlations are quite sensitive to coordinate rotation (e.g., Smith 1981). Nonetheless, the smaller (than for $v$) absolute values of $u$ correlation can be treated as a reliable observational result. However, the observed zero-crossing scale of the $u$ correlation is subject to wide uncertainty: anywhere from 8 to 40 km (Fig. 12, right panel). Yet, this zero crossing is absolutely to be expected for correlations of velocity perpendicular to the separation vector (e.g., Batchelor 1960). That the zero crossing is clearly resolved in the numerical model results is a reflection of better statistics and an
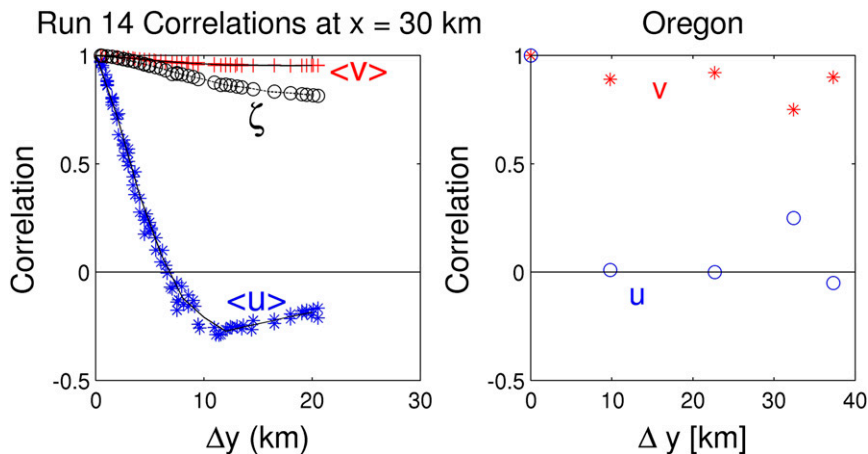


FIG. 12. (left) Correlation as a function of alongshore separation $\Delta y$ at $x = 30$ km for run 14. Individual correlation values are shown by symbols, and the solid lines represent averaging all values within a 2-km bin. Correlations are plotted for depth-averaged cross-shelf velocity (blue asterisks), depth-averaged alongshore velocity (red plus symbols), and free-surface height (black circles). (right) Correlations of midshelf velocity components vs alongshore lag on the Oregon continental shelf, after Kundu and Allen (1976). The comparison is meant to be only qualitative.
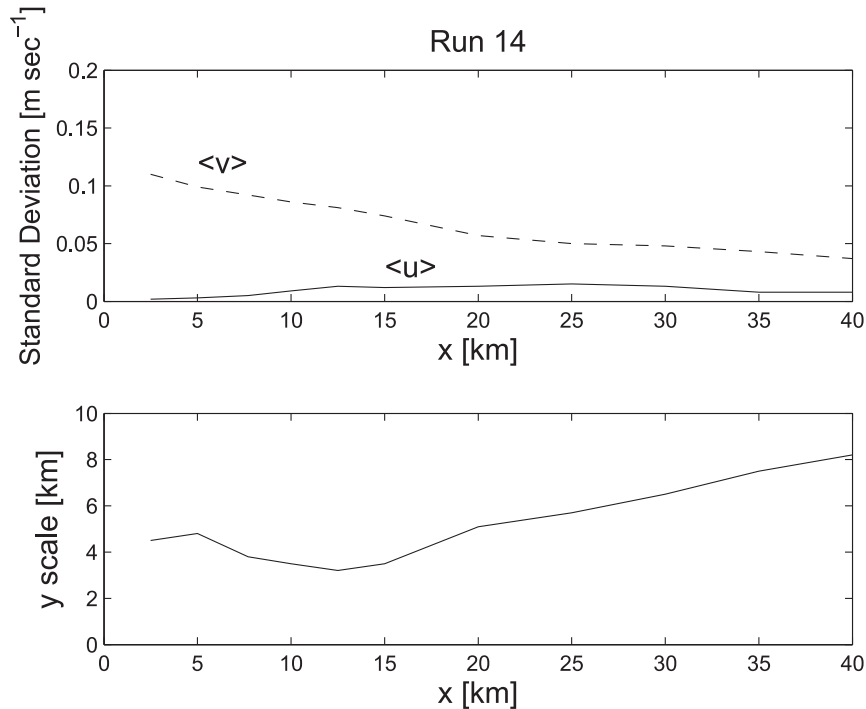
FIG. 13. Results from run 14, calculated for days 350–500. (top) Standard deviations of depth-averaged alongshore and cross-shelf velocity as a function of distance offshore. (bottom) Correlation length scale (defined as the lag distance to the first zero crossing) for depth-averaged cross-shelf currents as a function of distance offshore. Sea level and alongshore currents are correlated over far greater scales at all $x$.

unambiguous coordinate system (to define the cross-shelf direction) rather than any peculiarity of the cyclic coordinate system. An exact comparison is not to be expected given the differing geometries and the idealized, monochromatic nature of the present wind forcing. These points will be addressed in a future study.

### c. Parameter variations

While the qualitative behavior of run 14 is to be found in all the runs summarized in Table 1, results for peak eddy energy levels and wavelengths are clearly dependent on model parameters. A few sensitivities are apparent simply by comparing runs that are matched except for a single parameter differing.

For example, $EKE_M$ increases with stratification (cf. runs 11, 12, and 8) and with the wind forcing amplitude (run 2 vs 10). Further, the instability is more energetic for longer forcing periods (run 1 vs 5 and 23 vs 27) and smaller Coriolis parameter (run 10 vs 25). Not surprisingly, the instability is less energetic with larger friction, although an order of magnitude increase in $r$ only brings about a 50% $EKE_M$ reduction (run 23 vs 24 and run 20 vs 21). The effect of bottom slope appears more ambiguous; comparing runs 10 and 26 suggests that an

increasing bottom slope allows a more energetic instability, but a comparison of runs 27 and 29 suggests that results are insensitive. The sign of the wind stress (hence initial upwelling vs downwelling) is important in that $\tau_A < 0$ runs take much longer to equilibrate than do paired $\tau_A > 0$ runs. Although both signs lead to similar wavelengths (runs 14 vs 16 and 6 vs 17), the $\tau_A > 0$ runs lead to higher $EKE_M$.

The dominant wavelength at the time of EKE maximum $\lambda_M$ also reveals some patterns. For example, the wavelength increases with decreased $f$ (runs 10 vs 25) and decreased bottom slope (runs 10 vs 26 and 29 vs 27). Also, the wavelength increases with increasing forcing period (runs 5 vs 1 and 27 vs 23). The wavelength does not appear to have any systematic relation with initial stratification (runs 11, 12, and 8), forcing amplitude (run 2 vs 10), or bottom friction (run 23 vs 24 and run 20 vs 21). The lack of an obvious dependence on stratification is perhaps surprising because one would expect that the length scale associated with baroclinic instability would scale as the internal Rossby radius of deformation, although by the time $EKE_M$ is reached, length scales have evidently evolved as part of a turbulent inverse cascade. This issue will be clarified in the following scalings.

## 4. Scalings

### a. Maximum eddy kinetic energy

Following the arguments in B16, we might expect that the maximum spatially averaged eddy kinetic energy $EKE_M$ would depend on the available potential energy generated during a forcing cycle and on the scaled bottom slope $s$ (i.e., slope Burger number) because it affects the overall stability properties. In addition, it seems reasonable to expect that there is a dependence on the forcing frequency compared to the eddy energy growth rate, roughly $\sigma \approx a_3 s^{-1} f$ [$a_3 = O(0.002)$] based on B16 [his (21)]. Specifically, one might expect that if the growth rate is slow relative to the forcing period, there would not be time for the instability to develop before conditions change. Finally, the qualitative comparisons in the preceding section suggest that there is some dependency on the bottom friction.

First, a rough scaling for spatially averaged available kinetic energy over the inner portion of the shelf is taken to be

$$E_0 \approx \alpha N^2 |\tau_A| (2\rho_0 \omega f)^{-1} \qquad (6)$$

based on B16, his (16), and the wind duration $\Delta t$ is replaced with $\omega^{-1}$. Further, as in B16, it will be assumed that the eventual maximum EKE is proportional to the APE. B16 finds that there were two multiplicative corrections that could then be applied to this first estimate of APE [(6)]: one reflecting the effect of scaled bottom slope on APE generation and another reflecting the instability growth rate. Both of these corrections are of the form $(1 + b_1 s^2)^{-1}$, and the exact value of the constant $b_1$ is a function of whether upwelling-favorable or downwelling-favorable winds have been applied. For the present model runs, it appears that in all cases the maximum EKE always occurs near the end of the upwelling phase of the forcing (even when the run is initialized with downwelling: $\tau_A < 0$). Thus, a similar correction in terms of $s$ is attempted here.

Next, one might expect that the energy released would depend on the forcing frequency compared to the growth rate. For example, a function of frequency and growth rate in the form

$$[1 + b_2(\omega\sigma^{-1})^2]^{-1} \approx [1 + b_2(\omega s f^{-1})^2]^{-1} \qquad (7)$$

might be expected to be a reasonable multiplicative correction because energy would decrease for higher forcing frequencies. This form, however, is very similar to the suggested $(1 + b_1 s^2)^{-1}$ correction except for the ratio $\omega f^{-1}$, so that this might be expected to be somewhat redundant.

Finally, a frictional correction is also anticipated, and this ought to take the form of a ratio of the forcing frequency $\omega$ to a frictional decay rate $rh^{*-1}$, where $h^*$ is a representative water depth. The choice of $h^*$ is not particularly obvious, but a first estimate would be the depth of the offshore edge of the inner shelf zone where the water has all been replaced via Ekman transport:

$$h^* = [\alpha |\tau_A| (\rho_0 \omega f)^{-1}]^{1/2}, \qquad (8)$$

a form adapted from B16 [his (8)]. A functional form for this multiplicative correction to (6) that inhibits $EKE_M$ for strong friction but leaves it unaffected for weak friction is then

$$(1 + b_3 rh^{*-1}\omega^{-1})^{-1}. \qquad (9)$$

Exploration of different powers of $(rh^{*-1}\omega^{-1})$ show that this linear dependence appears best.

Thus, taken together, the expected form of the scaling for $EKE_M$ is

$$EKE_M$$
$$\approx a_1 E_0 (1 + b_1 s^2)^{-1} [1 + b_2(\omega s f^{-1})^2]^{-1} (1 + b_3 rh^{*-1}\omega^{-1})^{-1}. \qquad (10)$$

The coefficients $a_1$, $b_1$, $b_2$, and $b_3$ are all found empirically by minimizing the least squares errors between the estimate (10) and the numerical model results. The resulting best fit yields $a_1 = 0.072$, $b_1 = 10$, $b_2 = 7$, and $b_3 = 0.1$. This fit has an rms error of $8.81 \times 10^{-5}\,m^2\,s^{-2}$ and a correlation of 0.93. Experimentation shows, however, that setting $b_2 = 0$ (i.e., dropping the growth time correction) yields a fit nearly as good (rms error of $8.82 \times 10^{-5}\,m^2\,s^{-2}$ and correlation of 0.93). Leaving out the frictional correction ($b_3 = 0$) increases the error by 13% and dropping the bottom slope correction ($b_1 = 0$, $b_3 \neq 0$) increases the error by 56%. Thus, a reasonable scaling for maximum spatially averaged eddy kinetic energy is

$$EKE_M \approx a_1 E_0 (1 + b_1 s^2)^{-1}(1 + b_3 rh^{*-1}\omega^{-1})^{-1}, \qquad (11)$$

with $a_1 = 0.071$, $b_1 = 10$, and $b_3 = 0.1$. This outcome is interesting in that there is a meaningful frictional contribution, but B16, using finite duration wind forcing, does not detect a substantial $EKE_M$ dependence on the bottom friction.

### b. Alongshore wavelength

Not surprisingly, the alongshore wavelength at peak EKE in Table 1, $\lambda_M(x_M, t_M)$, is well correlated with the alongshore correlation length scale for cross-shelf flow. Specifically, the alongshore correlation scale $L_u^y$ (defined

as the first zero crossing of the $\langle u \rangle$ correlation function; about 7 km in Fig. 12) at $x = x_M$ is computed for the last 60 days of each model run. This scale is correlated at 0.84 with $\lambda_M$, and the regression slope is 0.2 (i.e., $\lambda_M$ is typically a factor of 5 larger than the correlation scale). In most baroclinic instability problems, one might expect the initial wavelength to be related to the internal Rossby radius of deformation, with, potentially, corrections due to the effect of the bottom slope. In the present problem, however, the initial instability is expected to be followed, to some extent, by a turbulent evolution that is likely to be strongly affected by the oscillating background environment. Thus, the ultimate length scale may not strongly reflect an initial Rossby radius scale.

The near-surface concentration of eddy kinetic energy (e.g., Fig. 9) suggests that a reasonable starting estimate for $\lambda_M$ might nonetheless be an internal Rossby radius based on the thickness of the surface mixed layer, that is,

$$Nh_{\text{mix}}f^{-1}, \tag{12}$$

where $h_{\text{mix}}$ is the thickness of the near-surface boundary layer. This can be estimated based on the Pollard et al. (1972) depth:

$$h_{\text{PRT}} = u^*(fN)^{-1/2}, \tag{13}$$

where $u^* = (|\tau_A|\rho_0^{-1})^{1/2}$ is a friction velocity based on the surface wind stress [model results show that (13) does correlate reasonably, 0.68, with the calculated mixed layer depth at $t = t_M$]. In addition, it seems plausible also to include multiplicative corrections for the scaled bottom slope $s$ and the forcing frequency relative to the growth rate. The resulting scaling to be tested is

$$\lambda_M \approx a_2[|\tau_A|N(\rho_0 f)^{-1}]^{1/2}f^{-1}(1 + c_1 s^2)^{-1}[1 + c_2(\omega sf^{-1})^2]^{-1}, \tag{14}$$

where $a_2$, $c_1$, and $c_2$ are to be found by minimizing rms errors. Once again, it is found that allowing $c_2 \neq 0$ only improves the fit by 1%, and so we take $c_2 = 0$, that is, we again neglect the explicit correction for growth rate relative to forcing frequency. The final scaling is thus

$$\lambda_M \approx a_2[|\tau_A|N(\rho_0 f)^{-1}]^{1/2}f^{-1}(1 + c_1 s^2)^{-1}. \tag{15}$$

With $a_2 = 12.3$ and $c_1 = 0.6$, the error of the fit is 3.05 km, and the correlation is 0.84. If $c_1 = c_2 = 0$, the error of the fit increases by 37%.

If the growth rate correction in (14) is retained, but the scaled bottom slope correction is deleted, the fit improves considerably compared to dropping both corrections, but the result is not quite as good as if $c_1 \neq 0$ and

$c_2 = 0$ (e.g., 2% vs 1% increase in error relative to using both corrections for $\lambda_M$). Thus, it is marginal as to which of these corrections to retain and which to drop. However, including both really appears to be redundant: why include both corrections when the error reduction is only a further 1%? Dropping the growth time correction, then, does not unambiguously mean that the correction is not physically important but only that it is not proven important by the runs on hand.

## 5. Discussion

The results presented here demonstrate that for every arrangement of parameters attempted, spatially uniform, fluctuating alongshore winds lead to baroclinic instability in a stratified coastal ocean. The important conclusion is that even when winds reverse direction regularly, hence constraining the growth of available potential energy, the system remains unstable at all times regardless of the wind direction. The growing instability evidently prevents available potential energy from growing indefinitely (albeit slowly) as in the two-dimensional case. It is important to point out that the equilibrated system is more unstable during the upwelling-favorable phase of the wind than during the downwelling-favorable phase. Instabilities develop most strongly when wind forcing has longer periods, so that one might expect a relative insensitivity to higher-frequency wind forcing if spectrally broadband winds were applied. Perhaps the most satisfying outcome of this study is that the Kundu and Allen (1976) correlation versus separation diagram is qualitatively reproduced for the entire range of parameters treated (e.g., Fig. 12). As anticipated kinematically, the correlation diagram indeed reflects the differing scales associated with large-scale alongshore flow and with smaller-scale instabilities that dominate cross-shelf velocity. Finally, it is worth pointing out that the pleasing result expressed by Fig. 12 is unambiguously related to baroclinic instability; the potentially complicating effects of irregular topography or spatial wind variations (for example) are clearly not required.

While these findings are suggestive that wind-forced baroclinic instability is likely to be a rather universal process over a stratified continental shelf, they are far from conclusive. Questions remain as to how stratified shelf systems respond to realistically random alongshore wind forcing and to the inclusion of a realistic time-mean wind. Further, it is desirable to evaluate the results in the context of more realistic shelf slope topographies. In particular, one might ask how shelf eddy generation due to baroclinic instability compares to the anticipated complex flow patterns in the presence of realistic alongshore

topographic variability. These issues are presently being treated and will be reported on in the future.

## REFERENCES

Barth, J. A., 1989a: Stability of a coastal upwelling front: 1. Model development and stability theorem. *J. Geophys. Res.*, **94**, 10 844–10 856, doi:10.1029/JC094iC08p10844.

——, 1989b: Stability of a coastal upwelling front: 2. Model results and comparison with observations. *J. Geophys. Res.*, **94**, 10 857–10 883, doi:10.1029/JC094iC08p10857.

——, 1994: Short-wavelength instabilities on coastal jets and fronts. *J. Geophys. Res.*, **99**, 16 095–16 115, doi:10.1029/94JC01270.

Batchelor, G. K., 1960: *Theory of Homogeneous Turbulence.* Cambridge University Press, 197 pp.

Beardsley, R. C., D. C. Chapman, K. H. Brink, S. R. Ramp, and R. Schlitz, 1985: The Nantucket Shoals Flux Experiment (NSFE79). Part I: A basic description of the current and temperature variability. *J. Phys. Oceanogr.*, **15**, 713–748, doi:10.1175/1520-0485(1985)015<0713:TNSFEP>2.0.CO;2.

Brink, K. H., 2011: Topographic rectification in a stratified ocean. *J. Mar. Res.*, **69**, 483–499, doi:10.1357/002224011799849354.

——, 2016: Continental shelf baroclinic instability. Part I: Relaxation from upwelling or downwelling. *J. Phys. Oceanogr.*, **46**, 551–568, doi:10.1175/JPO-D-15-0047.1.

——, and S. J. Lentz, 2010: Buoyancy arrest and bottom Ekman transport. Part II: Oscillating flow. *J. Phys. Oceanogr.*, **40**, 636–655, doi:10.1175/2009JPO4267.1.

——, and D. A. Cherian, 2013: Instability of an idealized tidal mixing front: Symmetric instabilities and frictional effects. *J. Mar. Res.*, **71**, 227–252, doi:10.1357/002224013807719473.

Dever, E. P., 1997: Subtidal velocity correlation scales on the northern California shelf. *J. Geophys. Res.*, **102**, 8555–8572, doi:10.1029/96JC03451.

Durski, S. M., and J. S. Allen, 2005: Finite-amplitude evolution of instabilities associated with the coastal upwelling front. *J. Phys. Oceanogr.*, **35**, 1606–1628, doi:10.1175/JPO2762.1.

Flierl, G. R., and J. Pedlosky, 2007: The nonlinear dynamics of time-dependent subcritical baroclinic currents. *J. Phys. Oceanogr.*, **37**, 1001–1021, doi:10.1175/JPO3034.1.

Haidvogel, D. B., H. G. Arango, K. Hedstrom, A. Beckmann, P. Malanotte-Rizzoli, and A. F. Shchepetkin, 2000: Model evaluation experiments in the North Atlantic basin: Simulations in nonlinear terrain-following coordinates. *Dyn. Atmos. Oceans*, **32**, 239–281, doi:10.1016/S0377-0265(00)00049-X.

Kuebel Cervantes, B. T., J. S. Allen, and R. M. Samelson, 2003: A modeling study of Eulerian and Lagrangian aspects of shelf circulation off Duck, North Carolina. *J. Phys. Oceanogr.*, **33**, 2070–2092, doi:10.1175/1520-0485(2003)033<2070:AMSOEA>2.0.CO;2.

Kundu, P. K., and J. S. Allen, 1976: Some three-dimensional characteristics of low-frequency current fluctuations near the Oregon coast. *J. Phys. Oceanogr.*, **6**, 181–199, doi:10.1175/1520-0485(1976)006<0181:STDCOL>2.0.CO;2.

Loder, J. H., 1980: Topographic rectification of tidal currents on the sides of Georges Bank. *J. Phys. Oceanogr.*, **10**, 1399–1416, doi:10.1175/1520-0485(1980)010<1399:TROTCO>2.0.CO;2.

Pollard, R. T., P. B. Rhines, and R. O. R. Y. Thompson, 1972: The deepening of the wind-mixed layer. *Geophys. Fluid Dyn.*, **4**, 381–404, doi:10.1080/03091927208236105.

Smith, R. L., 1981: A comparison of the structure and variability of the flow field in three coastal upwelling regions: Oregon, northwest Africa, and Peru. *Coastal Upwelling*, F. A. Richards, Ed., Amer. Geophys. Union, 107–118.

Wijesekera, H. W., J. S. Allen, and P. Newberger, 2003: A modeling study of turbulent mixing over the continental shelf: Comparison of turbulent closure schemes. *J. Geophys. Res.*, **108**, 3103, doi:10.1029/2001JC001234.

Winant, C. D., 1983: Longshore coherence of currents on the southern California shelf during the summer. *J. Phys. Oceanogr.*, **13**, 54–64, doi:10.1175/1520-0485(1983)013<0054:LCOCOT>2.0.CO;2.

Winters, K. R., P. N. Lombard, J. J. Riley, and E. A. D'Asaro, 1995: Available potential energy and mixing in density-stratified fluids. *J. Fluid Mech.*, **289**, 115–128, doi:10.1017/S002211209500125X.